Applied Surface Science 663 (2024) 160214

Contents lists available at ScienceDirect

Applied Surface Science

journal homepage: www.elsevier.com/locate/apsusc

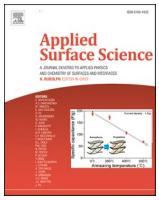

Full Length Article

Effect of multi-walled carbon nanotubes properties on the photocatalytic activity of bismuth-based composites synthesised via an imidazolium ionic liquid

Aleksandra Bielicka–Giełdoń [a,*], Patrycja Wilczewska [a], Monika Paszkiewicz [a], Anna Malankowska [a], Karol Szczodrowski [b], Jacek Ryl [c], Ewa Maria Siedlecka [a]

[a] Faculty of Chemistry, University of Gdansk, Wita Stwosza 63, 80-308 Gdansk, Poland
[b] Faculty of Mathematics, Physics and Informatics, University of Gdansk, Wita Stwosza 57, 80-308 Gdansk, Poland
[c] Faculty of Applied Physics and Mathematics, Gdansk University of Technology, Narutowicza 11/12, 80-233 Gdansk, Poland

ARTICLE INFO

Keywords:
Multi-walled carbon nanotubes
Ionic liquid
Bismuth oxybromide
Photocatalysis

ABSTRACT

The use of various types of multi-walled carbon nanotubes in the synthesis of bismuth oxybromide semiconductors via imidazolium ionic liquid was studied in detail. The effect of the MWCNT shape, specific surface area, and various diameters on the morphology, surface properties and photoactivity of the Bi-based composites has been investigated for the first time. So far, the literature has only shown the enhancement of photocatalytic activity of composites containing MWCNT; however, our research shows a broader view of the issue. The photocatalytic activity of the individual composites under UV–Vis irradiation was assessed by the degradation of various micropollutants, showing the diversity of properties of the obtained composites. It is also significant that in the composite system, the imidazolium ionic liquid played a crucial role in the formation of microspheres and acted as a dispersing agent, leading to an even distribution of MWCNTs on the surface of the spherical bismuth oxybromide.

1. Introduction

The optimal design of efficient photocatalysts is crucial to achieving a high-efficiency photocatalytic process. Therefore, preparing highly efficient photocatalysts for environmental applications is still challenging. Among the all-developed photocatalysts, bismuth-based semiconductor materials, such as BiOX (X = Cl, Br and I), Bi_2O_3, $Bi_2O_2CO_3$, BiOCOOH, $Bi_4Ti_3O_{12}$, have attracted considerable interest and are widely used as photocatalysts due to the unique construction, properties, and stability [1–7]. Among the bismuth-based photocatalysts, bismuth oxyhalides (BiOX) have been considered the most prospective ones. This new type of semiconductor material has potential photocatalysis applications because of its unique and excellent electrical and optical properties [1,3,8–12]. Among BiOX catalysts, bismuth oxybromide is of great research interest because it is an active and stable visible-light photocatalyst with advantageous performance under visible-light irradiations. BiOBr is an important V–VII ternary compound which crystallises in the tetragonal matlockite structure. The layer structure is characterised by $[Bi_2O_2]$ slabs interleaved by double slabs of halogen atoms. However, its photocatalytic activity has been limited by the high recombination of its photogenerated electron-hole pairs [1,8,13–16].

One of the outstanding strategies to enhance the photocatalytic activity of studied hetero-nanostructures was to recognise the construction of multi-walled carbon nanotubes (MWCNTs)/semiconductor composites. MWCNTs have been widely reported to synergistically enhance the photocatalytic activity of semiconductors through high-surface-area and high-quality active sites, retardation of electron-hole recombination and absorption under visible light by modification of bandgap and/or sensitisation of semiconductor [2–4,8–10,17–24]. Furthermore, MWCNTs provide scope for greater control of composite morphology, and the large specific surface area of MWCNTs can additionally support the photocatalysis process by outstanding adsorption of organic pollutants [25]. In view of the merits pointed out, MWCNTs can modify various photocatalysts to enhance photocatalytic performance by facilitating the separation rate of the photoinduced carriers. Carbon nanotubes have various electronic, thermal, and structural properties that change depending on nanotubes' different varieties. The properties are

* Corresponding author.
E-mail address: a.bielicka-gieldon@ug.edu.pl (A. Bielicka–Giełdoń).

https://doi.org/10.1016/j.apsusc.2024.160214
Received 19 January 2024; Received in revised form 12 April 2024; Accepted 4 May 2024
Available online 4 May 2024

defined by their geometrical parameters (e.g., shape, diameter, length, chirality, or twist) and the presence of functional groups (e.g., OH, —COOH, —NH_2) [17,26]. Although its properties can significantly affect the photocatalytic activity obtained, a random type of nanotubes has been usually used for investigations. Up till now, the study on composites containing MWCNTs with predetermined only one of the parameters such as the specific surface area [3], functionalised group [8,10,18], length [19], or diameter [20] has been shown. In many reports, the precise characterisation of MWCNTs has been omitted, while without detailed information about the nanostructures used, it is difficult to compare the results with the literature data. Recently, numerous carbon nanotubes/semiconductor composites with various activities have been developed, including MWCNTs/BiOCOOH [2], MWCNTs/BiOCl [3,20,21], MWCNTs/$Bi_2O_2CO_3$ [4], MWCNT/BiOBr [8,10], MWCNTs/$Bi_4O_5Br_2$ [18], MWCNT/BiOI [19]. While many attempts have been devoted to connecting bismuth-based semiconductors with carbon nanotubes, the performance of hetero-nanostructure photocatalysts remains largely unexplored.

The critical issues to solve in hybrid preparation are the influence of the thermal conductivity of CNTs on the synthesis of hybrid CNTs/semiconductors and the proper dispersion of CNTs on the surface of the semiconductor. The thermal conductivity of CNTs can directly influence the photocatalytic performance of BiOX, such as crystalline and indirect morphology, surface area, etc. [27]. On the other hand, the dispersity of MWCNTs on the photocatalyst surface may limit the use of their electron-conducting ability and cause a shielding effect [17,21]. Therefore, it is crucial to understand the influence of photocatalyst synthesis on their physicochemical and photocatalytic activity.

Recent studies have demonstrated that ionic liquids (ILs) played an essential role in the controlled preparation of different inorganic functional nanomaterials [1,28–33]. The ionic liquid can act as a solvent, reactant, template, and carbon nanotube dispersing agent [8]. Most commonly used for photocatalysts' synthesis ILs with high solubility and high thermal and electrochemical stability are imidazolium (im) salts mainly containing 3-octyl-1-methylimidazoliom ($omim^+$) cation [21] and 3-heksadecyl-1-methylimidazolium ($C16mim^+$) cation [8]. Physiochemical proprieties of ILs can be designed by pairing an imidazolium cation with an appropriate anion in salt [1,8,28]. Our previous study [1] showed that 3-butyl-1-methylimidazoliom cation ($bmim^+$) with X^- as an anion (where X is Cl, Br) led to the elevation of photocatalytic activity of Bi-based materials by the specific surface development as they were used as a halide source in synthesis. ILs can also participate in synthesis as a dispersing agent of carbon material on photocatalyst surfaces [8,21].

The main aim of our work is to assess the effect of shape (among them the cylindrical and helical MWCNTs), specific surface area (in the range from 30 to 500 m^2g^{-1}), and diameter of multi-walled carbon nanotubes on the crystallinity, morphology, and photoactivity of the MWCNT/$Bi_4O_5Br_2$ composites. For the first time, the series of MWCNTs/$Bi_4O_5Br_2$ with various shapes and types of MWCNTs were used to prepare composites via the solvothermal method in glycerol and imidazolium ionic liquid – bmimBr. The physicochemical, optical, and photocatalytic activity of the prepared composites were compared. In our investigations, bmimBr played a double role as a dispersing agent and source of bromide ions. BmimBr was proposed by us as the template of $Bi_4O_5Br_2$ microspheres formation with the well-developed surface and simultaneously as a dispersing agent to solve the agglomeration problem MWCNTs on the surface of flower-like $Bi_4O_5Br_2$. The different photocatalytic oxidative and reductive activities of the individual MWCNTs/$Bi_4O_5Br_2$ composites were evaluated by the degradation of various micropollutants (5-fluorouracil, rhodamine B, and hexavalent chromium) under UV–vis and visible irradiation.

2. Experimental

2.1. Materials and sample preparation

The chemical reagents in the present work were analytical grade and used without further purification. The ionic liquid 1-butyl-3-methylimidazolium bromide (bmimBr) was purchased from Merck. Bismuth nitrate pentahydrate $Bi(NO_3)_3{\cdot}5H_2O$ and 5-fluorouracil (5-FU) were purchased from Aldrich, potassium bromide (KBr), and nitro blue tetrazolium chloride (NBT) from Alfa Aestar. Terephthalic acid (TA) was obtained from Hardon Scientific.

The multi-walled carbon nanotubes used in the research (Table 1) were purchased from Cheap Tubes Inc.

The commercial 10 mg of MWCNTs were purified in 10 ml 3 M HNO_3 to remove the content of metal catalysts and amorphous carbon [25,34]. The purified MWCNTs were washed with doubly distilled water and oven-dried at 105 °C overnight. MWCNTs/$Bi_4O_5Br_2$ nanocomposites were prepared using ionic liquid-assisted two-step solvothermal methods. The first stage included solvothermal synthesis complex precursor, and the second was hydrolysis.

In a typical synthesis, 2 mmol of $Bi(NO_3)_3{\cdot}5H_2O$ and 2 mmol of bmimBr were dissolved in 20 mL of glycerol, respectively. Next, 2.5 % (12.5 mg) of various MWCNTs were added to the bismuth precursor solution. All nanocomposites were prepared with 2.5 % wt. of multi-walled carbon nanotubes selected based on literature [35]. Then, the mixture was sonicated for 30 min to obtain a homogeneous phase. After that, the bmimBr solution was added into the solution with MWCNTs dropwise under constant stirring at room temperature. The obtained mixture was sonicated for 60 min to ensure the reactants had an excellent dispersion and was then transferred into a 50 mL Teflon-lined stainless autoclave. The solvothermal reaction was conducted at 160 °C for 16 h. After that, the autoclave was naturally cooled to room temperature. Finally, the residue was washed with ethanol three times and dried at 80 °C overnight. The hydrolysis process was based on our previous report [1,28]. For comparison, pure $Bi_4O_5Br_2$ was prepared under the same conditions. The labels of nanocomposite samples were listed in Table 2.

2.2. Characterization

The X-ray powder diffraction (XRD) data was collected from a Bruker D2 Phaser by high-intensity Cu-Kα with a wavelength of 1.5406 Å. The chemical states of the samples were analysed using XPS (ThermoFisher Scientific Escalab 250Xi). The morphologies were characterised by scanning electron microscopy (JOEL JSM-7610F FEG-SEM) and transmission electron microscopy (TEM, Tecnai Spirit Biotwin) performed at 120 kV. The diffuse reflectance spectra (DRS) were measured on a UV–Vis spectrophotometer (UV-2600 UV–VIS Spectrometer Shimadzu), using $BaSO_4$ as the reference at room temperature. The scanning range was from 250 to 700 nm. The band gap energy value was calculated using the Kubelka–Munk plot. Photoluminescence spectra of samples were recorded from 300 to 700 nm at room temperature using Perkin Elmer-LS-550B with an excitation wavelength of 315 nm. The elemental

Table 1
Studied multi-walled carbon nanotubes (MWCNTs) without functionalisation.

Label	Shape/size	Length	Outer diameter	Specific surface area
h_MWCNTs	helical (h)	1–10 μm	100–200 nm	30 m^2/g
l_MWCNTs	cylindrical/ medium (m)	10–20 μm	50–80 nm	60 m^2/g
m_MWCNTs	cylindrical/large (l)	10–30 μm	10–20 nm	233 m^2/g
s_MWCNTs	cylindrical/small (s)	10–30 μm	< 8 nm	500 m^2/g

Table 2
Sample label of prepared $Bi_4O_5Br_2$ and MWCNTs/ $Bi_4O_5Br_2$ composites samples.

No.	Sample label	Source of halogen	MWCNTs type	Outer diameter [nm]	MWCNTs [%]
1.	$Bi_4O_5Br_2$	IL: BmimBr	without MWCNTs	–	0
2.	s_MWCNT/ $Bi_4O_5Br_2$		Small (s)	<8	2.5
3.	m_MWCNT/ $Bi_4O_5Br_2$		Medium (m)	10–20	2.5
4.	l_MWCNT/ $Bi_4O_5Br_2$		Large (l)	50–80	2.5
5.	h_MWCNT/ $Bi_4O_5Br_2$		Helical (h)	100–200	2.5

analysis determined the total carbon and nitrogen in the MWCNTs/ $Bi_4O_5Br_2$ in Elemental Analyzer Vario El Cube CHNS Elementar. The thermogravimetric analysis (TGA, TG209 Netzsch) was conducted to determine the real content of MWCNTs in the prepared MWCNTs-$Bi_4O_5Br_2$ at a heating rate of 10 °C/min from ambient temperature to 800 °C in argon. Gas nitrogen adsorption and desorption isotherms were measured at 77 K using a Micromeritics ASAP 2020 system. Prior to measurements, the obtained samples were outgassed overnight under a vacuum at 473 K. The specific surface area (SSA) was determined based on the Braunauer-Emmet-Teller (BET) model, taking a cross-sectional area of 0.162 nm^2 per nitrogen molecule. The average pore diameter was determined on the basis of the desorption branches of the nitrogen isotherms using the Barrett-Joyner-Halenda (BJH) method.

2.3. Photocatalytic activity measurement

The photocatalytic experiments under UV–Vis irradiation were performed based on the previous report [1]. The concentration of photocatalysts, volume of solution, and sample collection were similar to the previously described photocatalytic degradation of 5-fluorouracil (5-FU) and rhodamine B (RhB), and photoreduction of chromium(VI) [1,28]. In the RhB and 5-FU degradation tests, 3 mg of photocatalysts was added to 15 ml (0.2gL^{-1}) of RhB or 5-FU solution at a concentration of 15 mgL^{-1}. The initial pH of the solutions was 6.5. For the Cr(VI) degradation experiments, 7.5 mg of the photocatalyst was dispersed in 15 ml (0.5gL^{-1}) of Cr(VI) solution of concentration 20 mgL^{-1} and pH 3. The suspension was stirred in the dark for 30 min to establish the adsorption–desorption equilibrium on the surface of the photocatalyst. The photocatalytic processes were performed under UV–vis irradiation at room temperature using a 150 W medium-pressure mercury Heraeus lamp as the light source. At the appropriate time intervals, 1 ml of suspension was taken, and nanoparticles were removed by filtration (5FU) or centrifugation (RhB and Cr(VI)) and analysed. The Cr(VI) concentration was measured according to ISO PN-EN 18,412 with a 1,5-diphelynocarbazide method. Rhodamine B concentration was determined by UV–vis spectrophotometry at 554 nm (Perkin Elmer Lambda XLS+). The 5-FU concentration was measured using HPLC Perkin Elmer Series 200 with UV–vis detector and C-18 reverse-phase column (150 mm x 4.6 nm, 2.6 μm, Phenomenex). The mobile phase was water and acetonitrile (V: V = 2:98), a flow rate was 0.5 mL min^{-1}, and wavelength detection was at 266 nm.

Additionally, photocatalytic activity under visible light toward cytostatic drug 5-FU was conducted. Sunset CPS + solar simulator (Atlas Matrial Testing Technology LLC) equipped with the cooling system, a 1700 W Xe lamp as the light source with filter cut-off 420 nm was used. The initial concentration of photocatalysts and pharmaceuticals remained unchanged [1]. In the experiments under visible light, the temperature was maintained at 25 °C.

To verify the generation of superoxide anion radicals ($^{\bullet}O_2^-$) and hydroxyl radicals ($^{\bullet}OH$) during irradiation of MWCNTs/$Bi_4O_5Br_2$ nitroblue tetrazolium chloride (NBT) and terephthalic acid (TA) were used, respectively. The concentration of NBT was $2.5\bullet10^{-5}$ M, and TA was $5\bullet10^{-4}$ M in a $2.0\bullet10^{-3}$ M NaOH solution. The production of superoxide anion radicals was analysed by detecting the absorption decrease of NBT at 259 nm. The photoluminescence of 2-hydroxy terephthalic acid (HTA), a product of reaction TA with $^{\bullet}OH$, was measured from 300 nm to 700 nm, and the excitation wavelength was 300 nm.

3. Results and discussion

3.1. Chrystal structures characterisation

3.1.1. XRD

The XRD patterns of the pure $Bi_4O_5Br_2$ and the series of MWCNTs/ $Bi_4O_5Br_2$ samples synthesised using various types of MWCNTs were depicted in Fig. 1.

The diffraction pattern of $Bi_4O_5Br_2$ was indexed to a monoclinic $Bi_4O_5Br_2$ (PDF 00-037-0699 card). However, when multi-walled carbon nanotubes were added to the synthesis, apart from the $Bi_4O_5Br_2$ phase, characteristic diffraction peaks of the metallic Bi^0 phase (PDF 00-044-1246) were also observed. These results could be explained by converting Bi^{3+} ions to metallic Bi^0 via a redox reaction with MWCNTs. This phenomenon was also observed in other carbonaceous materials [36,37] and at high temperatures during the solvothermal synthesis of semiconductors [38]. The shape, diameter, specific surface area, and localisation of MWCNTs in the MWCNTs/$Bi_4O_5Br_2$ composite influenced the ability of the reduction process. The appearance of the Bi^0 phase in s_MWCNTs/$Bi_4O_5Br_2$ and h_MWCNTs/$Bi_4O_5Br_2$ composites was observed. For m_MWCNTs/$Bi_4O_5Br_2$ and l_MWCNTs/$Bi_4O_5Br_2$ materials, the Bi^0 phase was even more visible. (Fig. 1).

In addition to the metallic bismuth phase in composites obtained using MWCNTs, the appearance of the $Bi_{24}O_{31}Br_{10}$ phase was also observed. This phase is closely related to the transformation of bismuth oxybromide $Bi_4O_5Br_2$ under heating in the presence of MWCNTs, highly heat-conducting materials. Furthermore, the thermal conductivity of MWCNT is highly dependent on size and decreases with increasing the diameter of MWCNT [27]. Thus the high temperature of synthesis caused local overheating of the solution and the formation of the $Bi_{24}O_{31}Br_{10}$ phase (PDF 04-011-3959) [39,40,41,42,43]. The influence of highly thermally conductive materials in synthesising the crystalline phase of photocatalysts was not considered and studied in the literature. Moreover, no typical XRD patterns of MWCNTs were observed in studied nanocomposites, which may occur due to the low content and well-dispersed MWCNTs in the prepared photocatalysts. A similar phenomenon was also observed in the literature [21,35].

3.1.2. XPS

The surface chemical composition of prepared nanocomposites MWCNTs/$Bi_4O_5Br_2$ was investigated by analysing XPS spectra. The survey spectra (Fig. 2a) showed the peaks corresponding to C, Bi, O, and Br.

Fig. 2b shows the high-resolution Bi 4f spectra with two signals located at 164.2 eV and 158.9 eV (sample $Bi_4O_5Br_2$) related to Bi's binding energy $4f_{7/2}$ and Bi $4f_{5/2}$ electrons confirming Bi^{3+} state of bismuth were shown [38]. Compared to the binding energy of Bi^{3+} of pure $Bi_4O_5Br_2$, MWCNTs/$Bi_4O_5Br_2$ signals shifted to higher energy 164.8 eV and 159.5 eV, indicating the chemical environment of Bi had changed, and carbon form MWCNTs interacted with bismuth in $Bi_4O_5Br_2$. The bismuth element in our work mainly existed in the trivalent form. Moreover, the chemical interaction of multi-walled carbon nanotubes with the phase of $Bi_4O_5Br_2$ confirmed that electron/hole separation between these materials could occur during the photocatalytic process [3]. The presence of metallic bismuth in nanocomposites was not observed on XPS spectra. The results suggested that the reduction reaction of Bi^{3+} to Bi^0 by carbon nanotubes occurred locally in the first step of the solvothermal synthesis. Then, bismuth oxyhalides were formed on the Bi^0 phase, preventing XPS analysis

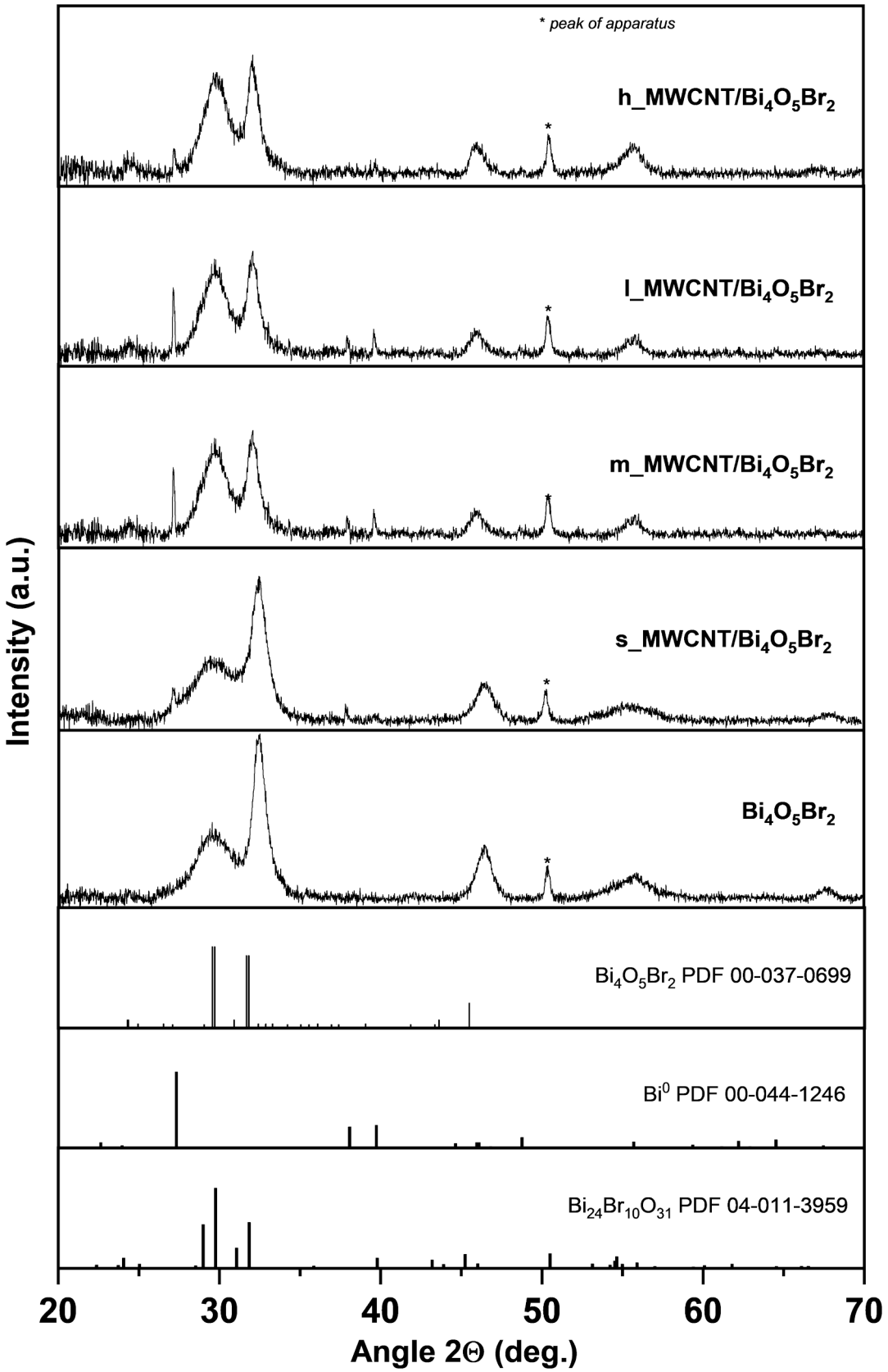

Fig. 1. XRD pattern of MWCNTs/$Bi_4O_5Br_2$ composites with different multi-walled carbon nanotubes (MWCNTs 2,5% wt.).

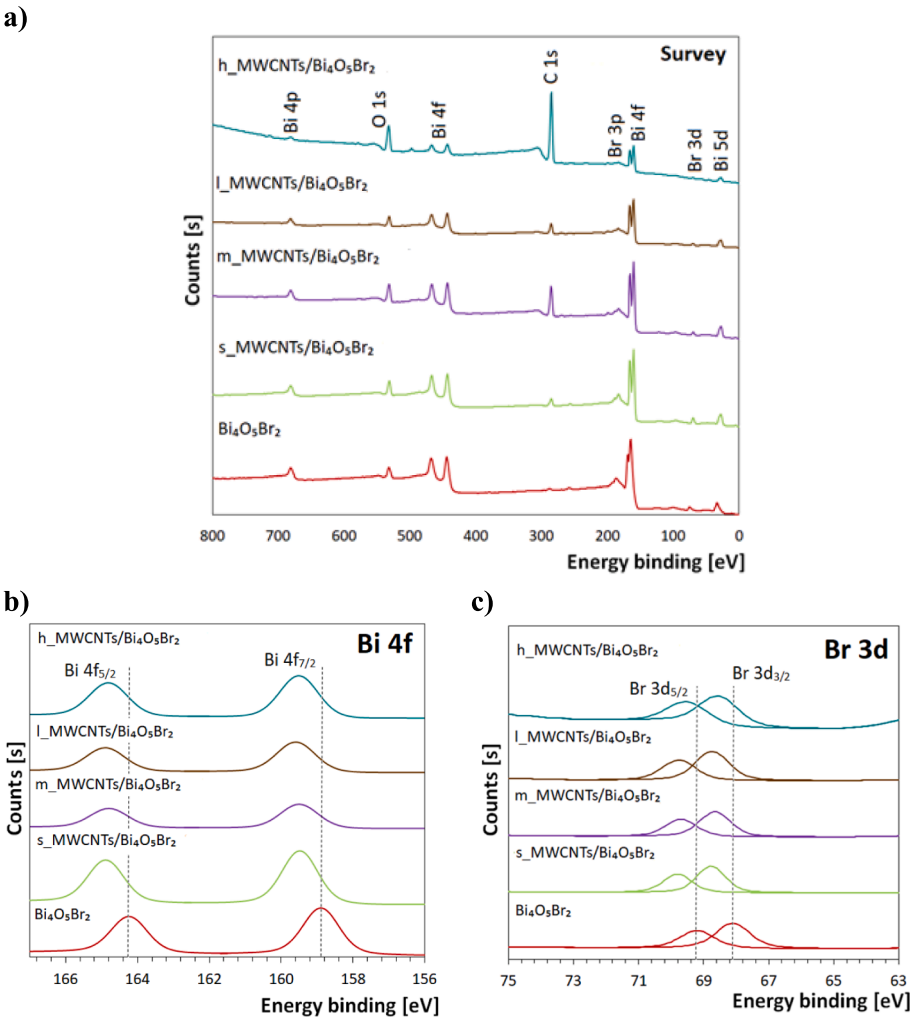

Fig. 2. a) survey xps and high-resolution spectra of b) bi 4f and c) br 3d of prepared photocatalysts.

detection of metallic bismuth. In the Br 3d spectra (Fig. 2c), the binding energies of 68.1 eV and 69.2 eV for pure $Bi_4O_5Br_2$ and 68.7 eV and 69.7 eV for nanocomposites were attributed to Br $3d_{5/2}$ and $3d_{3/2}$, respectively, which could be assigned to bromine in the monovalent oxidation state [38]. The peaks of Br $3d_{5/2}$ and $3d_{3/2}$ of nanocomposites shifted due to the atom's environment (the electronegativity of carbon is lower than oxygen). The peaks corresponding to N were not found by the XPS analysis, confirming that the ionic liquid used for the synthesis was utterly washed out during synthesis, as was reported before [1].

3.1.3. *SEM/TEM*

The SEM and TEM observed the samples' morphologies and presented in Fig. 3. Results indicated that the size of multi-walled carbon nanotubes impacted the crystallinity and size of particles of l_MWCNT/$Bi_4O_5Br_2$ samples. Pristine $Bi_4O_5Br_2$ possessed hierarchical micro flower-like particles with well-assembled and closed-packed nanosheets. The s_MWCNT/$Bi_4O_5Br_2$ composite displayed similar structures, but flower-like microspheres were two times smaller than pristine bismuth-rich oxybromide.

SEM and TEM images confirmed that s_MWCNTs did not wrap around $Bi_4O_5Br_2$. Due to the nanotube's small size, carbon material between the plates interfered with self-assembling particles. The samples prepared with medium and large MWCNTs were characterised by more complex microspheres built from irregular particles of identical thick nanosheets. The m_MWCNT and l_MWCNTs were well attached, embedded, and interwoven on the surface of $Bi_4O_5Br_2$. The introduction of helical MWCNTs to $Bi_4O_5Br_2$ resulted in assembling nanosheets into similar microstructures as in the case of large and medium MWCNTs. The interaction of helical carbon structure with forming nanosheets during synthesis resulted in the formation of nanoplates smaller and thicker than in the case of m_MWCNT/$Bi_4O_5Br_2$ and l_MWCNT/$Bi_4O_5Br_2$.

Additionally, the amorphous structures appeared in the h_MWCNTs/$Bi_4O_5Br_2$ sample, while the absence of these structures in the case of samples synthesised using small, medium, and large MWCNTs was found. Changes in the photocatalyst structure in the presence of MWCNTs in the BiOBr/MWCNT composite were also observed by the Hernádi group. They noticed the interference effect of multi-walled carbon nanotubes on the synthesis. MWCNTs induced higher crystallinity but lower photoactivity of BiOBr/MWCNT composites [44].

It is worth mentioning that the size of the nanocomposite particles significantly depended on the type and size of multi-walled carbon nanotubes used in the synthesis. The size range particles of prepared photocatalysts were listed in Table 3. The l_MWCNT/$Bi_4O_5Br_2$ composite particles were four times bigger than s_MWCNT/$Bi_4O_5Br_2$ and about two times bigger than m_MWCNT/$Bi_4O_5Br_2$ and h_MWCNT/$Bi_4O_5Br_2$.

In the presented research, the bmimBr ionic liquid played a role in synthesis as a reagent, template, and dispersion agent. The results confirmed that imidazolium IL with the butyl chain was sufficient to obtain a good dispersion of MWCNTs. Moreover, no aggregation of carbon material was observed for all photocatalysts, confirming the

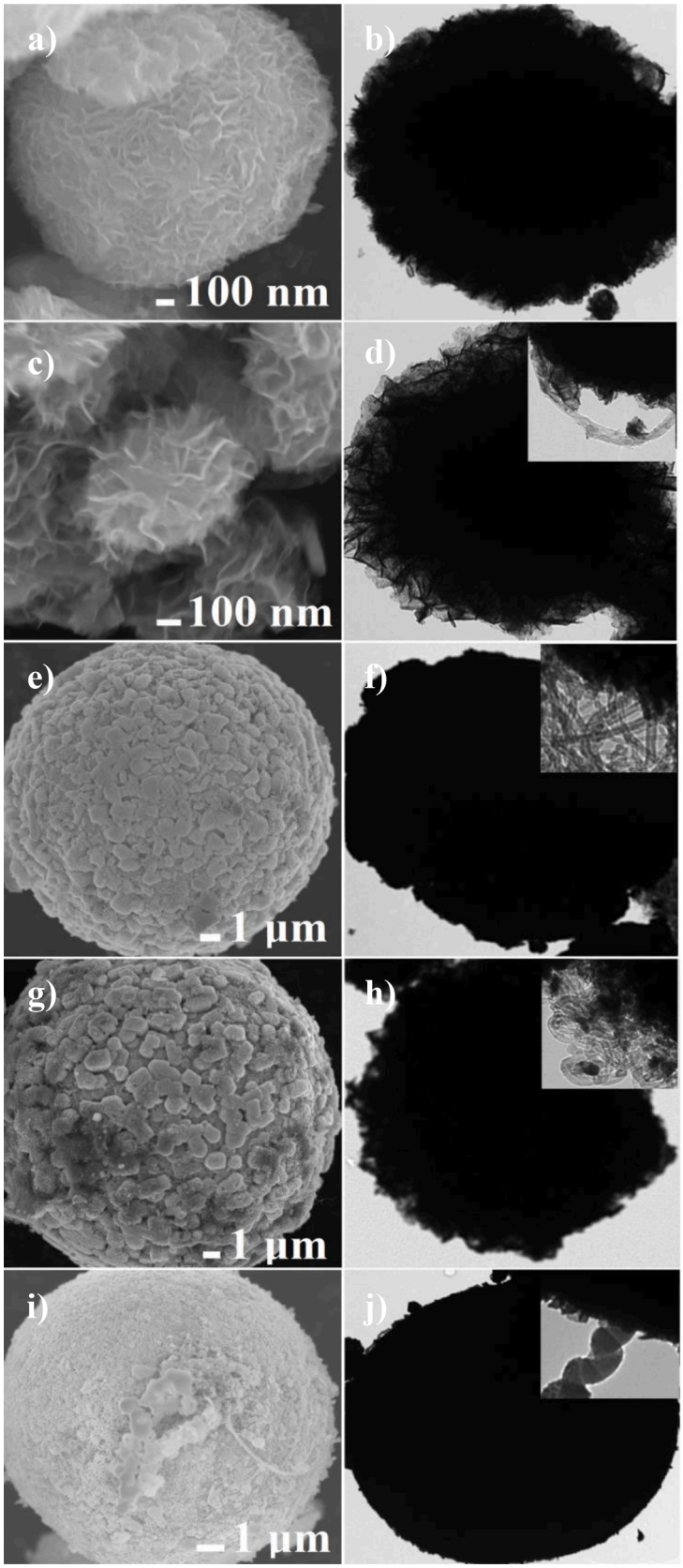

Fig. 3. Scanning and transmission electron microscopy (SEM, TEM) images of a,b) $Bi_4O_5Br_2$, c,d) s_MWCNT/$Bi_4O_5Br_2$; e,f) m_MWCNT/$Bi_4O_5Br_2$; g,h) l_MWCNT/$Bi_4O_5Br_2$ and i,j) h_MWCNT/$Bi_4O_5Br_2$.

Table 3
Summarised results of morphology, optical properties, and composition of prepared photocatalysts.

Sample label	Size range [μm]	Eg [eV]	TGA [%]	Elemental analysis [%]		
			MWCNTs	C	H	N
$Bi_4O_5Br_2$	2.13–4.10	2.91	0	1.16	0.32	0.04
s_MWCNT/ $Bi_4O_5Br_2$	0.68–1.26	2.85	2.89	3.73	0.44	0.09
m_MWCNT/ $Bi_4O_5Br_2$	18.0–27.8	2.68	2.78	3.92	0.25	0.05
l_MWCNT/ $Bi_4O_5Br_2$	22.4–51.7	2.52	3.82	4.4	0.27	0.04
h_MWCNT/ $Bi_4O_5Br_2$	18.0–34.2	2.57	2.56	3.97	0.31	0.04

ionic liquid's utility in this type of nanocomposites. The electron transport ability of the composite could be improved by the excellent dispersion of MWCNTs in photocatalytic materials. This phenomenon minimised the contact resistances among nanotubes due to the distance among individual tubes [45].

The addition of s_MWCNTs to the synthesis, which was a minor steric hindrance during the aggregation of nanosheets, caused the formation of loosely packed and smaller flower-like microspheres. It is well known that increasing particle size decreases specific surface area, reducing photocatalytic activity [46]. TEM images (Fig. 3) confirmed that $Bi_4O_5Br_2$ nanosheets built 3D architectures, and MWCNTs were on their surface. The carbon nanomaterial acted as a template and/or steric hindrance.

3.1.4. TGA and elemental analysis

The presence of carbon in the prepared nanocomposites tested by TGA and elemental analysis was consistent. A TGA analysis was carried out to estimate the MWCNTs' content in the MWCNTs/$Bi_4O_5Br_2$ nanocomposite. The weight loss at the temperature range of 450–650 °C corresponded to the thermal degradation of MWCNTs. Obtained weight losses were summarised in Table 3. Based on the results assessed, the content of MWCNTs in composites was close to the theoretical value of 2.5 % w/w, except l_MWCNTs/$Bi_4O_5Br_2$. Using the l_MWCNTs, a significant spherical hindrance in composites synthesis, the nanotube content in composite increased up to 3.8 %, with a simultaneous reduction in the $Bi_4O_5Br_2$ synthesis efficiency.

The elemental analysis confirmed the carbon content in samples and showed that the nitrogen content was trace. This fact suggested that imidazolium ionic liquid was removed from photocatalysts, which we reported earlier [1].

3.1.5. Uv–vis

Multi-walled carbon nanotubes can act as a photosensitiser to wider bandgap semiconductors [2,4] or as a carbon dopant through the covalent bond between MWCNTs and photocatalysts, causing narrowing of the energy bandgap [10,17], enhancing absorption of the visible light range. Such an enhancement of light collection intensity in the range above 400 nm increases the number of photogenerated electrons and holes that participate in the photocatalytic reaction and elevates the photocatalytic activity of semiconductors. The UV–Vis reflectance spectra studied MWCNTs/$Bi_4O_5Br_2$ nanocomposites were presented in Fig. 4.

MWCNTs/$Bi_4O_5Br_2$ nanocomposites exhibited higher light absorption in the visible range than pristine $Bi_4O_5Br_2$. Moreover, composites with medium, large, and helical MWCNTs were characterised by a redshift of the band edge of the absorption spectrum. Results suggested that the morphology of semiconductors in composite depends on the type of multi-walled carbon nanotube. It was closely related to augmenting the amount of MWCNTs placed on the surface, which increased light absorption intensity in the visible region. The redshift of band edge spectra for MWCNTs/$Bi_4O_5Br_2$ nanocomposites with large, medium, and helical multi-walled carbon nanotubes suggested the connection between these phases was different than in s_MWCNTs/$Bi_4O_5Br_2$.

Energy bandgaps (Eg) of the synthesised nanocomposites MNWCNTs/$Bi_4O_5Br_2$ were theoretically determined by the Kubelka–Munk function and presented in Table 3. The Eg values for nanocomposites were lower than the Eg value for pure $Bi_4O_5Br_2$ (2.9 eV), which complied with the literature [47,48] and confirmed the presence of MWCNTs on the surface of the prepared nanomaterials, which acted as a light absorber. The estimated values of Eg of the photocatalysts prepared with m_MWCNTs, l_MWCNTs, and h_MWCNTs were similar and amounted to 2.68 eV, 2.52 eV, and 2.57 eV, respectively. The similarity could also be found in their particles' morphology, especially their shape and size. Furthermore, s_MWCNT/$Bi_4O_5Br_2$ with Eg = 2.85 eV possessed the most promising Eg for visible light photocatalysis.

3.1.6. PL

The electron transport properties of carbon nanotubes are dependent on various factors such as adsorbed substance on the surface [49], type and pH solution in which carbon nanotubes are suspended [50], impurities content, size [45], length of individual tubes, and numbers of walls [51]. Carbon nanotubes with larger diameters exhibit lower transport

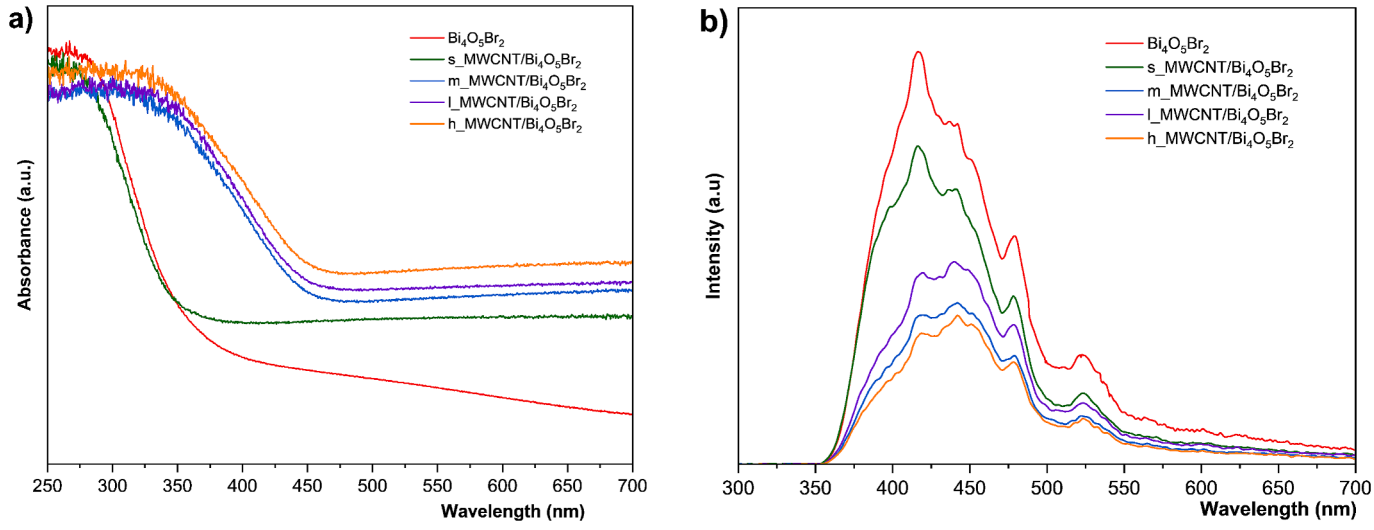

Fig. 4. a) uv–Vis reflectance spectra and b) PL spectra of studied MWCNTs/$Bi_4O_5Br_2$ nanocomposites with various sizes of MWCNTs with 2.5% wt. content.

barriers of electrons, resulting in a higher decrease in photoluminescence intensity (better electron transport, thus effective separation of photogenerated electrons) [52].

As shown in Fig. 4b, the $Bi_4O_5Br_2$ exhibited the highest photoluminescence intensity among the synthesised nanocomposites. The introduction of MWCNTs to composites caused a decrease in PL intensity. The most effective electron junction from $Bi_4O_5Br_2$ to MWCNTs was observed in m_MWCNT/$Bi_4O_5Br_2$ and h_MWCNT/$Bi_4O_5Br_2$ samples. It is worth noting that the shape of the PL spectra differed from those obtained for $Bi_4O_5Br_2$ and s_MWCNT/$Bi_4O_5Br_2$. This fact proved that the interaction between helical, large, and medium MWCNTs and $Bi_4O_5Br_2$ differed from that between s_MWCNTs and $Bi_4O_5Br_2$. However, the decrease in PL spectrum intensity of m_MWCNT/$Bi_4O_5Br_2$ and h_MWCNT/$Bi_4O_5Br_2$ could be connected with the poorer photogeneration of e^-/h^+ charge pairs. Therefore, the morphology of composites changed with the increase of the size of MWCNTs, and the decreasing intensity of PL for l_MWCNT/$Bi_4O_5Br_2$ could be caused by poorly crystallised areas $Bi_4O_5Br_2$ than by their effective separation and slower recombination of photogenerated e^-/h^+charge pairs.

3.1.7. BET

The porosity and the specific surface area (SSA) were studied by measuring gas N_2 adsorption at 77 K. Fig. 5 presents the adsorption/desorption isotherms of the pristine and multi-walled carbon nanotubes-modified bismuth oxybromide materials.

The presence of capillary condensation (a sharp increase in the value of the adsorbed amount) above $0.8p/p_0$ suggests the presence of pores with a relatively large volume. Taking into account the shape of the hysteresis loop, it can be assumed that $Bi_4O_5Br_2$ and s_MWCNT/$Bi_4O_5Br_2$ materials have a similar pore structure mainly based on the pores in the shape of slots, wedges (H3-type hysteresis loops), while the hysteresis loops of m_and l_MWCNT/$Bi_4O_5Br_2$ materials, indicate the presence of pores with a shape similar to cylinders/prisms characterized with non-uniform diameter (tilted H1-type loops). In the case of the h_MWCNT/$Bi_4O_5Br_2$ sample, the pore structure is more uniform, taking into account the pore diameters. However, the shape of pores can be related to the distorted cylinders. The values of SSA determined using the Braunauer-Emmet-Teller (BET) model and the average pore diameter determined using the Barrett-Joyner-Halenda (BJH) method were presented in Table 4.

When cylindrical multi-walled carbon nanotubes of different sizes (s, m and l) were used, a decrease in the specific surface area and average pore diameter of the obtained MWCNTs/$Bi_4O_5Br_2$ composites were observed in relation to pristine $Bi_4O_5Br_2$. For $Bi_4O_5Br_2$, the SSA was 74.2 m^2g^{-1}; for s_MWCNT/$Bi_4O_5Br_2$, it decreased to 62.6 m^2g^{-1}, and for m_and l_MWCNT/$Bi_4O_5Br_2$, a further decrease was observed, but the values were comparable and were 53.9 m^2g^{-1} and 56.2 m^2g^{-1} for m_and l_MWCNT/$Bi_4O_5Br_2$ composites, respectively. A significant increase in the specific surface area compared to pristine $Bi_4O_5Br_2$ was observed for the h_MWCNT/$Bi_4O_5Br_2$ composite, for which the SSA value increased to 121.1 m^2g^{-1}. Despite the largest specific surface area, the composite obtained with helical nanotubes was characterized by the smallest average pore diameter, 9 nm.

3.2. Photocatalytic activity of MWCNTs/$Bi_4O_5Br_2$ series of composites

3.2.1. The effect of the various types of MWCNTs on photocatalytic oxidation and reduction processes

The photocatalytic activity of synthesised composites was evaluated by removing rhodamine B, 5-fluorouracil, and chromium(VI) from aqueous solutions using artificial sunlight irradiation. The model compounds characterised the different physicochemical properties and investigated photo-oxidation and reduction properties of MWCNTs/$Bi_4O_5Br_2$ composites. RhB is frequently used in photocatalysis oxidation studies [1], but it can also act as a sensitiser and is characterised by a great affinity to photocatalyst surface. The photocatalytic oxidation study used 5-FU with low adsorption ability (the coefficient constant of octanol/water (logKo/w = -0.89). In contrast, chromium(VI), in the form of $Cr_2O_7^{2-}$ ions at pH = 3, was used to study a reduction process with photogenerated e^-.

The degradation efficiency of RhB, Cr(VI), and 5-FU in the photocatalytic process as a function of time under UV–Vis irradiation was illustrated in Fig. 6. Model compounds degradation data were well fitted to the pseudo-first-order model [1], expressed by the equitation $\ln(C/C_0) = kt$. The kinetics constants and regression coefficient of their removal were presented in Table 5.

3.2.1.1. Photooxidation of RhB. In the dark phase, the RhB adsorption onto the surface of studied photocatalysts (Fig. 6a) increased in the following order: $Bi_4O_5Br_2$ (20 %) < s_MWCNT/$Bi_4O_5Br_2$ (30 %) < m_MWCNT/$Bi_4O_5Br_2$ (40 %) < l_MWCNT/$Bi_4O_5Br_2$ (44 %) < h_MWCNT/$Bi_4O_5Br_2$ (68 %). The results indicated that the adsorption of RhB increased with the decrease of the specific surface of MWCNTs. The results conclude that the RhB adsorption at the surface of the composite was not connected with the adsorption at the MWCNTs surface. The crystalline form of $Bi_4O_5Br_2$ was the critical factor responsible for the adsorption of RhB.

RhB was degraded by no more than 20 % within 120 min of illumination without catalysts. The removal efficiency was enhanced in the presence of studied photocatalysts. In the light phase, RhB was oxidised after 45 min of illumination in the presence of s_MWCNT/$Bi_4O_5Br_2$, m_MWCNT/$Bi_4O_5Br_2$, and l_MWCNT/$Bi_4O_5Br_2$ photocatalysts, while under h_MWCNT/$Bi_4O_5Br_2$ composite RhB was utterly removed after 60 min of irradiation.

The degradation rate (k_{app}) of RhB in the presence of studied photocatalysts with cylindrical MWCNTs was higher than the k_{app} obtained for pure $Bi_4O_5Br_2$ (0.0711 min^{-1}) (Fig. 6a). It was found that the k_{app} decreased as the size of nanotubes increased. For s_MWCNT/$Bi_4O_5Br_2$, m_MWCNT/$Bi_4O_5Br_2$ and l_MWCNT/$Bi_4O_5Br_2$ was 0.1009 min^{-1}, 0.0979 min^{-1}, and 0.0967 min^{-1}, respectively. The highest RhB adsorption and presence of MWCNTs on the composite surface found for the h_MWCNTs sample likely shielded the photocatalyst towards sunlight and slowed down RhB oxidation. Due to this fact, the rate coefficient for composite with helical MWCNTs (h_MWCNT/$Bi_4O_5Br_2$ k_{app} 0.0631 min^{-1}) was lower than k_{app} for pure $Bi_4O_5Br_2$.

3.2.1.2. Photodegradation of 5-fluorouracil. The presence of anticancer drugs, whose representative is 5-fluorouracil, in the environment raises a significant concern due to their potentially negative impact on living organisms, as they cause, inter alia, teratogenic, mutagenic, and carcinogenic effects on growing cells. The 5-fluorouracil (5-FU) has been recently detected in different water compartments and hospital and municipal wastewaters, in concentrations ranging from $ng{\cdot}L^{-1}$ to $\mu g{\cdot}L^{-1}$ [25]. The release of 5-FU and other anticancer drugs in aquatic ecosystems can risk the ecological balance of natural environments. Hence, efficient methods for their removal from wastewater are required [25,28].

The photocatalytic activity of studied photocatalysts toward 5-FU cytostatic drug under UV–Vis and visible light was conducted. The adsorption of 5-FU varied from 0 to 10 %, indicating that adsorption in the dark phase was insignificant. In the absence of photocatalysts, 5-FU did not photolyse both under the UV–Vis and visible radiation. The removal efficiency was enhanced in the presence of photocatalysts in the studied systems.

3.2.1.2.1. Photodegradation of 5-FU under UV–vis light. The most spectacular effect in the 5-FU photodegradation under UV–vis light irradiation was observed for s_MWCNT/$Bi_4O_5Br_2$ composite (Fig. 6c). After 30 min of UV–Vis irradiation, 5-FU was degraded to 100 %. The degradation rate k_{app} was also the highest for s_MWCNT/$Bi_4O_5Br_2$ composite. Compared to the k_{app} of $Bi_4O_5Br_2$ photocatalyst without modification MWCNTs, the k_{app} for s_MWCNT/$Bi_4O_5Br_2$ composite

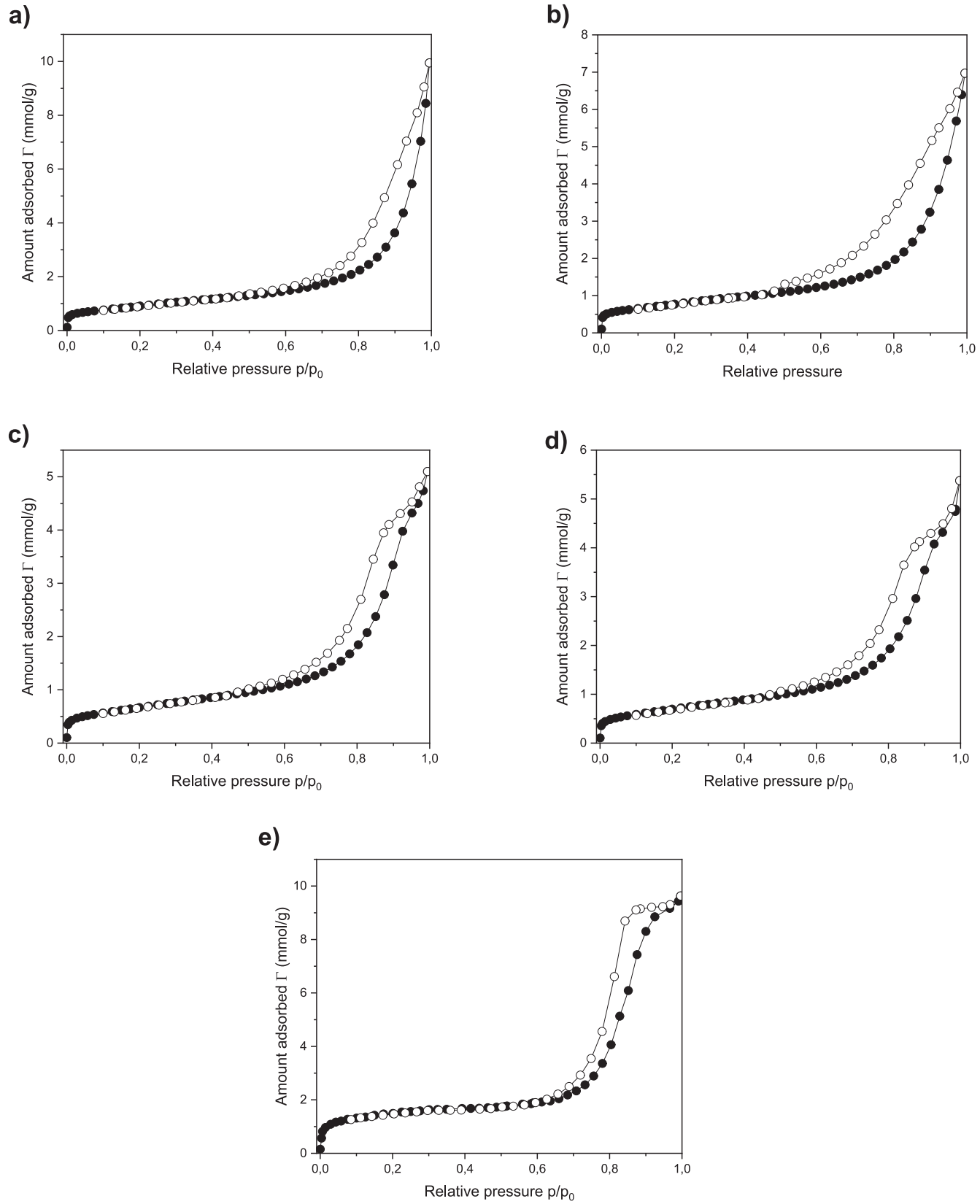

Fig. 5. Nitrogen adsorption (solid circles) – desorption (open circles) isotherms for the studied materials: a) $Bi_4O_5Br_2$, b) s_MWCNT/$Bi_4O_5Br_2$, c) m_MWCNT/$Bi_4O_5Br_2$, d) l_MWCNT/$Bi_4O_5Br_2$ and e) h_MWCNT/$Bi_4O_5Br_2$.

Table 4
Results of the BET and BJH analysis.

Sample name	Specific surface area [m^2g^{-1}]	Average pore diameter [nm]
$Bi_4O_5Br_2$	74.2	15
s_MWCNT/$Bi_4O_5Br_2$	62.6	10
m_MWCNT/$Bi_4O_5Br_2$	53.9	10
l_MWCNT/$Bi_4O_5Br_2$	56.2	10
h_MWCNT/$Bi_4O_5Br_2$	121.1	9

increased more than three times (Fig. 6c). For the $Bi_4O_5Br_2$ and s_MWCNT/$Bi_4O_5Br_2$, the decomposition rates were 0.0509 min^{-1} and 0.1655 min^{-1}, respectively. The h_MWCNT/$Bi_4O_5Br_2$ composite was also photoactive in drug degradation, and after 120 min of UV–vis radiation, about 98 % of the 5-FU was removed. However, the decomposition rate was lower than for s_MWCNT/$Bi_4O_5Br_2$ and $Bi_4O_5Br_2$ and was 0.0323 min^{-1}.

The composites with l_MWCNTs had lower activity (app. 50 % of 5-FU degraded after 120 min), probably due to rapid recombination at weakly crystallised sites and high electron availability (low transport

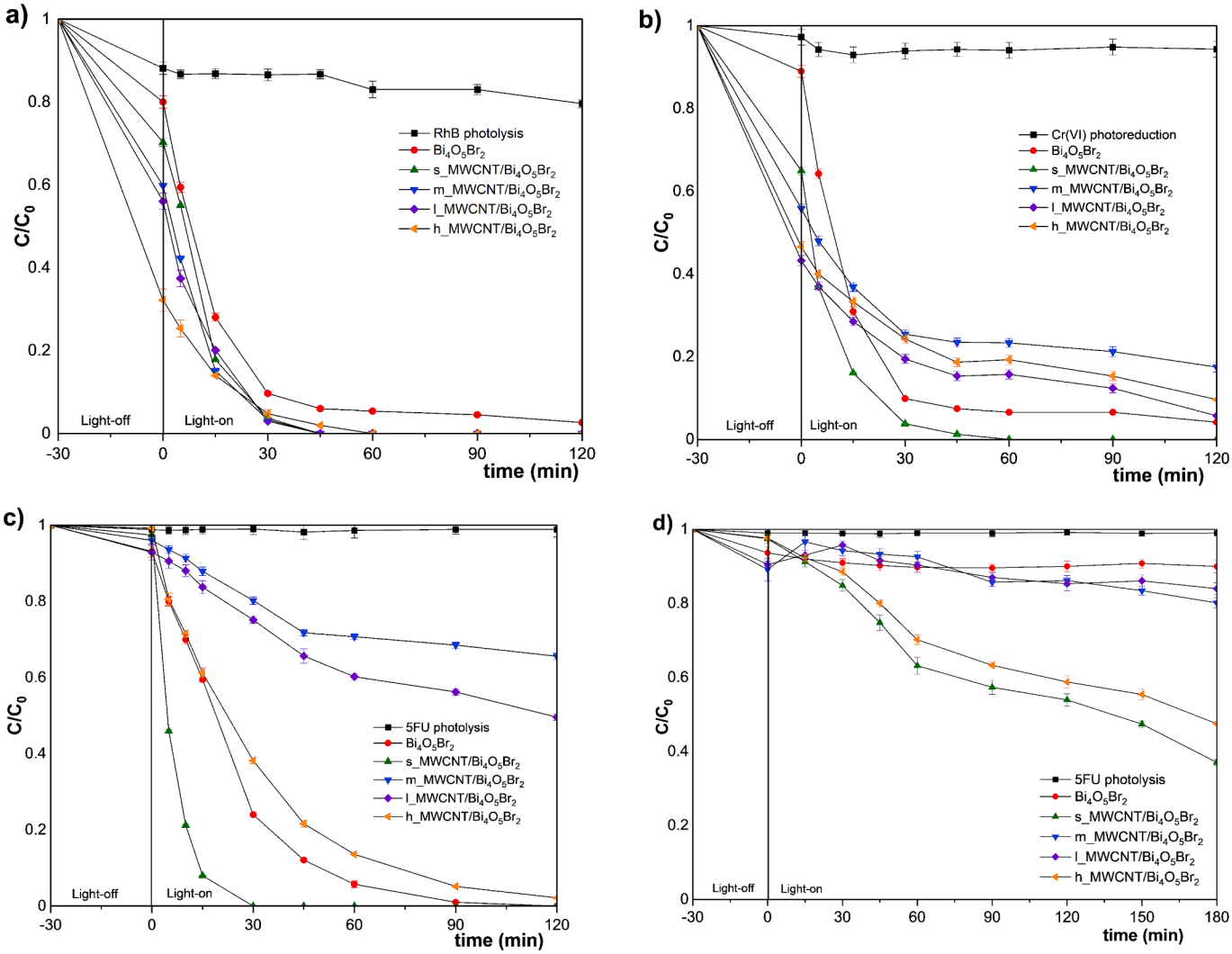

Fig. 6. Photocatalytic removal of RhB (a), hexavalent chromium (b), and 5-FU under UV–vis (c) and visible light (d) over MWCNTs/$Bi_4O_5Br_2$ composites.

Table 5
The kinetics constants and regression coefficient of selected micropollutant degradation.

Sample label	**RhB** (pH = 6.8)		**Cr(VI)** (pH = 3)		**5-FU** (pH = 6.4) **UV–vis (λ > 290 nm)**		**5-FU** (pH = 6.4) **Vis (λ > 420 nm)**	
	k [min^{-1}]	R^2	k [min^{-1}]	R^2	k [min^{-1}]	R^2	k [min^{-1}]	R^2
$Bi_4O_5Br_2$	0.0711	0.999	0.0738	0.999	0.0509	0.995	0.0007	0.952
s_MWCNT/$Bi_4O_5Br_2$	0.1009	0.993	0.0877	0.997	0.1655	0.996	0.0052	0.987
m_MWCNT/$Bi_4O_5Br_2$	0.0979	0.998	0.0260	0.999	0.0065	0.996	0.0011	0.962
l_MWCNT/$Bi_4O_5Br_2$	0.0967	0.995	0.0233	0.999	0.0075	0.996	0.0006	0.957
h_MWCNT/$Bi_4O_5Br_2$	0.0631	0.998	0.0200	0.996	0.0323	0.998	0.0040	0.985

barrier). The lowest photoactivity was observed for the composites with m_MWCNTs. Only approximately 34 % of 5-FU was degraded within 120 min.

3.2.1.2.2. Photodegradation of 5-FU under visible light. In the 5-FU degradation process under visible light, using various MWCNTs (Fig. 6d) for MWCNTs/$Bi_4O_5Br_2$ composites preparation increased the photocatalytic activity of bismuth-rich oxybromide. Only 10 % of 5-FU was removed using $Bi_4O_5Br_2$ without modification, but considering the 7 % adsorption of the drug, the material's photoactivity is negligible. Among the cylindrical MWCNTs, the smaller they were, the more effective the drug degraded. After 180 min of visible light irradiation, 5-FU was degraded in 16 %, 20 % and 63 % for l_MWCNT/$Bi_4O_5Br_2$, m_MWCNT/$Bi_4O_5Br_2$ and s_MWCNT/$Bi_4O_5Br_2$ composites, respectively. Using the composite with helical MWCNTs (h_MWCNT/$Bi_4O_5Br_2$), the efficiency of 5-FU decomposition significantly increased, and after 180 min of visible light irradiation, it achieved 53 %. The degradation rates (Table 5) were also the highest for s_MWCNT/$Bi_4O_5Br_2$ and h_MWCNT/$Bi_4O_5Br_2$ composites and were 0.0052 min^{-1} and 0.0040 min^{-1}, respectively.

3.2.1.3. Photoreduction of chromium(VI). In the absence of studied photocatalysts, Cr(VI) generally did not undergo photolytic reduction. Modification of $Bi_4O_5Br_2$ by various MWCNTs has contributed to increased chromium(VI) adsorption. The Cr(VI) adsorption onto the surface of MWCNTs/$Bi_4O_5Br_2$ composites with various types of MWCNTs (Fig. 6b), similar to rhodamine B sorption, increased in the following order $Bi_4O_5Br_2$ (11 %) < s_MWCNT/$Bi_4O_5Br_2$ (35 %) < m_MWCNT/$Bi_4O_5Br_2$ (44 %) < h_MWCNT/$Bi_4O_5Br_2$ (54 %) ≈ l_MWCNT/$Bi_4O_5Br_2$ (57 %) in the dark phase. Also, in this case, chromium(VI) adsorption did not correlate with the increase in the specific surface area of MWCNTs. Except for s_MWCNT/$Bi_4O_5Br_2$, the increase in adsorption did not contribute to increasing the efficiency of the photocatalytic process. Both the efficiency of chromium(VI) photodegradation and the decomposition rate were the most spectacular for the s_MWCNT/$Bi_4O_5Br_2$ composite (Fig. 6b). Only using s_MWCNT/$Bi_4O_5Br_2$ composite, a complete reduction of chromium(VI) was achieved after 60 min with the degradation rate 0.0877 min^{-1} (Table 5). The use of other photocatalysts allowed the photoreduction of chromium(VI) in 96 % for pristine $Bi_4O_5Br_2$, 94 % for l_MWCNT/$Bi_4O_5Br_2$, 90 % for h_MWCNT/$Bi_4O_5Br_2$ and 82 % for m_MWCNT/$Bi_4O_5Br_2$ composites within 120 min of the process. The photoreduction rates (k_{app}) of Cr(VI) for pristine $Bi_4O_5Br_2$ was 0.0738 min^{-1} and for other composites decreased as the size of the MWCNTs increased (Fig. 6b) and were 0.0260 min^{-1}, 0.0233 min^{-1}, 0.0200 min^{-1} for m_MWCNTs/$Bi_4O_5Br_2$, l_MWCNTs/$Bi_4O_5Br_2$, h_MWCNTs/$Bi_4O_5Br_2$, photocatalysts, respectively.

The results confirm the relationship observed on PL spectra and related to the ability to transport photo-excited electrons. As was noticed, the PL spectra shapes between helical, large, and medium MWCNTs and $Bi_4O_5Br_2$ were different than those obtained for pristine $Bi_4O_5Br_2$ and s_MWCNT/$Bi_4O_5Br_2$ (Fig. 6b). It can be concluded that electrons transferred to h_MWCNTs, l_MWCNTs and m_MWCNTs did not participate in the reduction process; therefore, it did not affect the effective reduction of hexavalent chromium despite increased sorption.

3.2.2. Production of hydroxyl ($^{\bullet}OH$) and superoxide radicals ($O_2^{\bullet-}$)

The formation of superoxide anion radicals ($O_2^{\bullet-}$) and hydroxyl radicals ($^{\bullet}OH$) during MWCNTs/$Bi_4O_5Br_2$ irradiation was verified to determine the photocatalytic degradation of pollutants. Experiments with the selected samples could explain the remarkable activity of s_MWCNT/$Bi_4O_5Br_2$ and h_MWCNT/$Bi_4O_5Br_2$.

The formation of the superoxide anion radicals under UV–vis and vis irradiation by synthesised photocatalysts was monitored by reaction with nitro blue tetrazolium chloride (NBT) as a probe molecule, which can readily react with $O_2^{\bullet-}$ to produce nitro blue tetrazolium formazan. The changes in concentration of NBT during irradiation were shown in Fig. 7.

Photogenerated electrons in the conduction band of pure $Bi_4O_5Br_2$ could react with O_2 dissolved in water and reduce it to $O_2^{\bullet-}$ which confirmed that the conduction band of bismuth-rich oxybromide is more negative than E^0 ($O_2/O_2^{\bullet-}$) (−0.046 V vs NHE). Furthermore, experiments conducted revealed the influence of MWCNT types on electron transport and separation in nanocomposites. The highest yield of $O_2^{\bullet-}$ generation was possessed by s_MWCNT/$Bi_4O_5Br_2$. The properties of s_MWCNTs indicated the highest transport barrier of electrons and the lowest separation ability of photogenerated charges among used multi-walled carbon nanotubes. However, the synergistic effect of morphology changes, the amount of generated superoxide anion radicals, and the ability to act as electrons sink can explain the excellent photocatalytic activity among prepared materials.

Additionally, m_MWCNT/$Bi_4O_5Br_2$ and h_MWCNT/$Bi_4O_5Br_2$ samples generated a similarly small amount of $O_2^{\bullet-}$ under UV–vis irradiation. Obtained superoxide anion radicals were related to higher capacity and faster electron transfer from $Bi_4O_5Br_2$ to MWCNTs, preventing their reaction with oxygen than s_MWCNTs. There was no $O_2^{\bullet-}$ in the system with l_MWCNT/$Bi_4O_5Br_2$_2.5, suggesting that large MWCNTs can receive and store electrons with higher efficiency.

The formation of $O_2^{\bullet-}$ under visible light was performed for nanocomposites which exhibited photocatalytic activity in this irradiation wavelength, such as s_MWCNT/$Bi_4O_5Br_2$ and h_MWCNT/$Bi_4O_5Br_2$. In the photocatalytic system with h_MWCNT/$Bi_4O_5Br_2$, the generation of $O_2^{\bullet-}$ has not occurred. Photogenerated electrons in lower numbers than under UV–vis were stored in h_MWCNTs, preventing reaction in O_2. On the other hand, nanocomposite s_MWCNT/$Bi_4O_5Br_2$ could produce superoxide anion radicals under visible light, contributing to high numbers of active sites and high s_MWCNTs transport barrier and efficiency sensibilisation of $Bi_4O_5Br_2$ by s_MWCNTs.

The results of the superoxide anion formation were consistent with PL and showed how important this issue is in nanocarbon composites. Furthermore, data agreed with photocatalytic activity and explained the difference in degradation efficiency of the selected micropollutants.

Reactions with terephthalic acid were performed to define if the photogenerated holes contributed to the formation of hydroxyl radicals. The fluorescence spectral results showed that pure $Bi_4O_5Br_2$ and MWCNTs/$Bi_4O_5Br_2$ composites cannot react with OH^-/H_2O to form $^{\bullet}OH$ during the photocatalytic process. Photodegradation of selected micropollutants occurred without these species.

3.2.3. The stability of s_MWCNT/$Bi_4O_5Br_2$ composite via 5-fluorouracil degradation

The stability test was performed for the most efficient s_MWCNT/$Bi_4O_5Br_2$ composite in photocatalytic degradation of 5-fluorouracil. The cycling experiment of s_MWCNT/$Bi_4O_5Br_2$ for photocatalytic 5-FU degradation was presented in Fig. 8.

During three consecutive photocatalytic cycles, a similar high degradation efficiency of 5-FU was achieved, and the drug was completely removed from the aqueous solution after 30 min of irradiation. In the fourth cycle, the efficiency decreased slightly to 91 % after 30 min of UV–Vis light exposure, and after 120 min, 5FU was still completely removed. This is confirmed by the relatively good stability of the obtained composite s_MWCNT/$Bi_4O_5Br_2$.

4. Conclusions

The results indicated that using various multi-walled carbon nanotubes in the solvothermal synthesis via an ionic liquid of MWCNTs/bismuth oxybromide composites significantly affected the morphology and properties of the obtained photocatalysts. MWCNTs influence the phase composition of the photocatalysts. When multi-walled carbon nanotubes were used for the synthesis, apart from the $Bi_4O_5Br_2$ phase, the metallic Bi^0 and $Bi_{24}O_{31}Br_{10}$ phases were also observed. The carbon

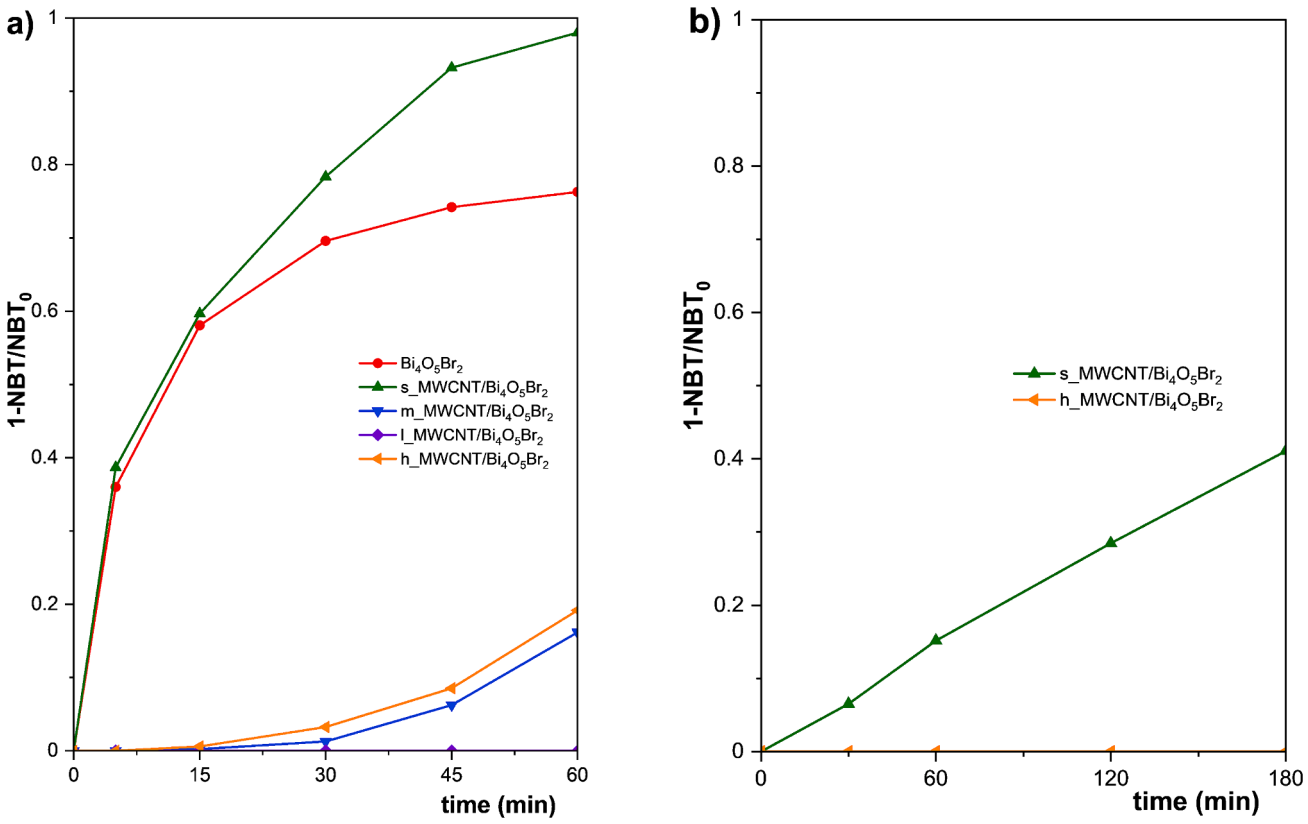

Fig. 7. Generation of superoxide radicals under a) UV–vis and b) vis irradiation in the presence of prepared photocatalysts.

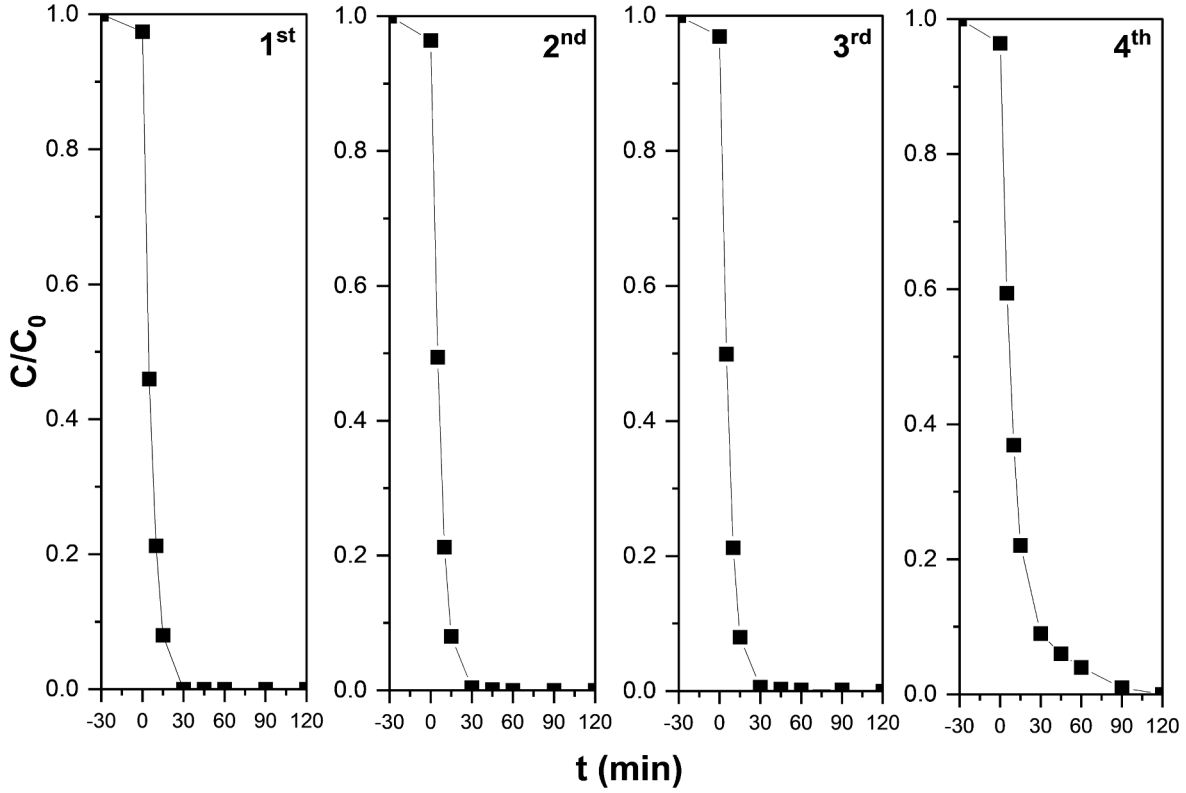

Fig. 8. Cyclings test for s_MWCNT/$Bi_4O_5Br_2$ composite *via* 5-FU degradation.

nanomaterial acted as a template and/or steric hindrance. The size and specific surface area of the nanocomposite particles significantly depended on the type and size of multi-walled carbon nanotubes used in the synthesis. When the smallest multi-walled carbon nanotubes (s_MWCNTs) were used, composite particles were smaller than pristine $Bi_4O_5Br_2$, while the other MWCNTs (m, l and h) were used, the particles were much larger. A decreased specific surface area of the obtained MWCNTs/$Bi_4O_5Br_2$ composites was observed in relation to pristine $Bi_4O_5Br_2$ (74.2 m^2g^{-1}) when cylindrical multi-walled carbon nanotubes of different sizes (s, m and l) were used while a significant increase in the specific surface area compared to pristine $Bi_4O_5Br_2$ was observed for the h_MWCNT/$Bi_4O_5Br_2$ composite (121.1 m^2g^{-1}).

The significant novelty of this research is that MWCNTs did not enhance the photocatalytic activity of every obtained bismuth-based composite for every pollutant. Results have shown that the effectiveness of the degradation process using MWCNTs/$Bi_4O_5Br_2$ composites significantly depended on the properties of the compound being removed. All obtained MWCNTs/$Bi_4O_5Br_2$ composites were more effective than pristine $Bi_4O_5Br_2$ only for dye rhodamine B degradation. In removing hexavalent chromium and the 5-fluorouracil drug, only the s_MWCNT/$Bi_4O_5Br_2$ composite was more effective than pristine $Bi_4O_5Br_2$. The highest degradation rate for each tested micropollutant (RhB, 5-FU, Cr(VI)) was obtained for a bismuth oxybromide composite with the smallest MWCNTs tested (s_MWCNT/$Bi_4O_5Br_2$).

In the presented research, the bmimBr ionic liquid played a role in synthesis as a reagent, template, and dispersion agent. The results confirmed that imidazolium IL with the butyl chain was sufficient to obtain a good dispersion of MWCNTs. Moreover, no aggregation of carbon material was observed for all photocatalysts, confirming the ionic liquid's utility in this type of nanocomposites. The electron transport ability of the composite could be improved by the excellent dispersion of MWCNTs in photocatalytic materials. This phenomenon minimised the contact resistances among nanotubes due to the distance among individual tubes.

CRediT authorship contribution statement

Aleksandra Bielicka–Giełdoń: Writing – review & editing, Writing – original draft, Visualization, Validation, Supervision, Resources, Project administration, Methodology, Investigation, Funding acquisition, Formal analysis, Data curation, Conceptualization. **Patrycja Wilczewska:** Writing – review & editing, Writing – original draft, Visualization, Validation, Methodology, Investigation, Formal analysis. **Monika Paszkiewicz:** Resources. **Anna Malankowska:** Investigation. **Karol Szczodrowski:** Investigation, Methodology. **Jacek Ryl:** Methodology, Investigation. **Ewa Maria Siedlecka:** Writing – review & editing, Writing – original draft, Supervision.

Declaration of competing interest

The authors declare that they have no known competing financial interests or personal relationships that could have appeared to influence the work reported in this paper.

Data availability

No data was used for the research described in the article.

Acknowledgements

This work was supported by the National Science Center (PL) [grant number DEC-2017/01/X/ST5/01136] and the Ministry of Education and Science (PL) [grant number DS 531-T020-D596-24].

References

[1] A. Bielicka-Giełdoń, P. Wilczewska, A. Malankowska, K. Szczodrowski, J. Ryl, A. Zielińska-Jurek, E.M. Siedlecka, Morphology, surface properties and photocatalytic activity of the bismuth oxyhalides semiconductors prepared by ionic liquid assisted solvothermal method, Sep. Purif. Technol. 217 (2019) 164–173, https://doi.org/10.1016/j.seppur.2019.02.031.
[2] S. Hu, S. Li, K. Xu, W. Jiang, J. Zhang, J. Liu, MWCNTs/BiOCOOH composites with improved sunlight photocatalytic activity, Mater. Lett. 191 (2017) 157–160, https://doi.org/10.1016/j.matlet.2016.12.077.
[3] D. Ma, J. Zhong, J. Li, C. Burda, R. Duan, Preparation and photocatalytic performance of MWCNTs/BiOCl: evidence for the superoxide radical participation in the degradation mechanism of phenol, Appl. Surf. Sci. 480 (2019) 395–403, https://doi.org/10.1016/j.apsusc.2019.02.195.
[4] X. Zhang, S. Li, S. Hu, J. Chen, W. Jiang, J. Zhang, L. Ji, L. Cai, Y. Wang, W. Song, J. Liu, Flower-like MWCNTs/$Bi_2O_2CO_3$ composites with enhanced photocatalytic activity under simulated solar light irradiation, Mater. Lett. 185 (2016) 50–53, https://doi.org/10.1016/j.matlet.2016.08.086.
[5] X. Liu, Z. Zhou, Y. Lu, T. Wang, P. Huo, Y. Yan, Increasing visible-light absorption for photocatalysis with black 2D $Bi_4Ti_3O_{12}$ nanosheets, Adv. Powder Technol. 30 (5) (2019) 1043–1050, https://doi.org/10.1016/j.apt.2019.02.019.
[6] D. Feng, X. Li, Y. Liu, X. Chen, S. Li, Emerging bismuth-based step-scheme heterojunction photocatalysts for energy and environmental applications, Renewables 1 (2023) 485–513, https://doi.org/10.31635/renewables.023.202300037.
[7] C. Wang, C. You, K. Rong, C. Shen, F. Yang, S. Li, An S-Scheme MIL-101(Fe)-on-BiOCl heterostructure with oxygen vacancies for boosting photocatalytic removal of Cr(VI), Acta Physico - Chimica Sinica 40 (7) (2024) 2307045, https://doi.org/10.3866/PKU.WHXB202307045.
[8] J. Xia, J. Di, S. Yin, H. Li, L. Xu, Y. Xu, C. Zhang, H. Shu, Improved visible light photocatalytic activity of MWCNT/BiOBr composite synthesized via a reactable ionic liquid, Ceram. Int. 40 (2014) 4607–4616, https://doi.org/10.1016/j.ceramint.2013.09.001.
[9] C.-W. Siao, H.-L. Chen, L.-W. Chen, J.-L. Chang, T.-W. Yeh, C.-C. Chen, Controlled hydrothermal synthesis of bismuth oxychloride/ bismuth oxybromide/ bismuth oxyiodide composites exhibiting visible-light photocatalytic degradation of 2-hydroxybenzoic acid and crystal violet, J. Colloid Interface Sci. 526 (2018) 322–336, https://doi.org/10.1016/j.jcis.2018.04.097.
[10] D. Liu, J. Xie, Y. Xia, Improved photocatalytic activity of MWCNT/BiOBr composite synthesized via interfacial covalent bonding linkage, Chem. Phys. Lett. 729 (2019) 42–48, https://doi.org/10.1016/j.cplett.2019.05.023.
[11] X. Meng, Z. Zhang, Bismuth-based photocatalytic semiconductors: Introduction, challenges and possible approaches, J. Mol. Catal. A Chem. 423 (2016) 533–549, https://doi.org/10.1016/j.molcata.2016.07.030.
[12] S. Li, C. Wang, K. Dong, P. Zhang, X. Chen, X. Li, MIL-101(Fe)/BiOBr S-scheme photocatalyst for promoting photocatalytic abatement of Cr(VI) and enrofloxacin antibiotic: performance and mechanism, Chin. J. Catal. 51 (2023) 101–112, https://doi.org/10.1016/S1872-2067(23)64479-1.
[13] J. Di, J. Xia, H. Li, S. Guo, S. Dai, Bismuth oxyhalide layered materials for energy and environmental applications, Nano Energy 41 (2017) 172–192, https://doi.org/10.1016/j.nanoen.2017.09.008.
[14] Z. Wang, M. Chen, D. Huang, G. Zeng, P. Xu, C. Zhou, C. Lai, H. Wang, M. Cheng, W. Wang, Multiply structural optimized strategies for bismuth oxyhalide photocatalysis and their environmental application, Chem. Eng. J. 374 (2019) 1025–1045, https://doi.org/10.1016/j.cej.2019.06.018.
[15] C.-S. Lu, Y.-J. Lai, J. Shaya, Y.-Y. Lin, F.-Y. Liu, J.-H. Lin, C.-W. Chen, H.-Y. Tsai, J.-W. Huang, C.-C. Chen, Fabrication and characterization of BiOxBry/BiOmIn coupled GCN heterojunctions with enhanced visible-light catalytic activity, Catal. Commun. 184 (2023) 106794, https://doi.org/10.1016/j.catcom.2023.106794.
[16] C.-C. Chen, S.-H. Chang, J. Shaya, F.-Y. Liu, Y.-Y. Lin, L.-G. Wang, H.-Y. Tsai, C.-S. Lu, Hydrothermal synthesis of BiOxBry/BiOmIn/GO composites with visible-light photocatalytic activity, J. Taiwan Inst. Chem. Eng. 133 (2022) 104272, https://doi.org/10.1016/j.jtice.2022.104272.
[17] K.K. Gangu, S. Maddila, S.B. Jonnalagadda, A review on novel composites of MWCNTs mediated semiconducting materials as photocatalysts in water treatment, Sci. Total Environ. 646 (2019) 1398–1412, https://doi.org/10.1016/j.scitotenv.2018.07.375.
[18] J. Di, M. Ji, J. Xia, X. Li, W. Fan, Q. Zhang, H. Li, $Bi_4O_5Br_2$ ultra small nanosheets in situ strong coupling to MWCNT and improved photocatalytic activity for tetracycline hydrochloride degradation, J. Mol. Catal. A Chem. 424 (2016) 331–341, https://doi.org/10.1016/j.molcata.2016.08.029.
[19] M. Su, C. He, L. Zhu, Z. Sun, C. Shan, Q. Zhang, D. Shu, R. Qiu, Y. Xiong, Enhanced adsorption and photocatalytic activity of BiOI–MWCNT composites towards organic pollutants in aqueous solution, J. Hazard. Mater. 229–230 (2012) 72–82, https://doi.org/10.1016/j.jhazmat.2012.05.061.
[20] S. Vadivel, J. Theerthagiri, J. Madhavan, T. Santhoshini Priya, N. Balasubramanian, Enhanced photocatalytic activity of degradation of azo, phenolic and triphenyl methane dyes using novel octagon shaped BiOCl discs/ MWCNT composite, Journal of Water, Process. Eng. 10 (2016) 165–171, https://doi.org/10.1016/j.jwpe.2015.12.001.
[21] S. Yin, J. Di, M. Li, W. Fan, J. Xia, H. Xu, Y. Sun, H. Li, Synthesis of multiwalled carbon nanotube modified BiOCl microspheres with enhanced visible-light response photoactivity, Clean – Soil, Air, Water 44 (7) (2016) 781–787, https://doi.org/10.1002/clen.201500418.
[22] H. Wang, H.L. Wang, W.F. Jiang, Solar photocatalytic degradation of 2,6-dinitro-p-cresol (DNPC) using multi-walled carbon nanotubes (MWCNTs)–TiO_2 composite

photocatalysts, Chemosphere 75 (2009) 1105–1111, https://doi.org/10.1016/j.chemosphere.2009.01.014.
[23] S. Perathoner, C. Ampelli, S. Chen, R. Passalacqua, D. Su, G. Centi, Photoactive materials based on semiconducting nanocarbons - a challenge opening new possibilities for photocatalysis, Journal of Energy Chemistry 26 (2017) 207–218, https://doi.org/10.1016/j.jechem.2017.01.005.
[24] D. Sudha, P. Sivakumar, Review on the photocatalytic activity of various composite catalysts, Chem. Eng. Process. 97 (2015) 112–133, https://doi.org/10.1016/j.cep.2015.08.006.
[25] M. Tański, J. Dołżonek, M. Paszkiewicz, J. Wojsławski, P. Stepnowski, A. Białk-Bielińska, Preliminary evaluation of the application of carbon nanotubes as potential adsorbents for the elimination of selected anticancer drugs from water matrices, Chemosphere 201 (2018) 32–40, https://doi.org/10.1016/j.chemosphere.2018.02.072.
[26] W.J. Lee, J.M. Lee, S.T. Kochuveedu, T.H. Han, H.Y. Jeong, M. Park, J.M. Yun, J. Kwon, K. No, D.H. Kim, S.O. Kim, Biomineralized N-doped CNT/TiO_2 core/shell nanowires for visible light photocatalysis, ACS Nano 6 (2012) 935–943, https://doi.org/10.1021/nn204504h.
[27] M.K. Samani, N. Khosravian, G.C.K. Chen, M. Shakerzadeh, D. Baillargeat, B. K. Tay, Thermal conductivity of individual multiwalled carbon nanotubes, Int. J. Therm. Sci. 62 (2012) 40–43, https://doi.org/10.1016/j.ijthermalsci.2012.03.003.
[28] P. Wilczewska, A. Bielicka-Giełdoń, A. Fiszka Borzyszkowska, J. Ryl, T. Klimczuk, E.M.a Siedlecka, Photocatalytic activity of solvothermal prepared BiOClBr with imidazolium ionic liquids as halogen sources in cytostatic drugs removal, J. Photochem. Photobiol. A: Chem. 382 (2019) 111932, https://doi.org/10.1016/j.jphotochem.2019.111932.
[29] Z. Li, Z. Jia, Y. Luan, T. Mu, Ionic liquids for synthesis of inorganic nanomaterials, Curr. Opin. Solid State Mater. Sci. 12 (1) (2008) 1–8, https://doi.org/10.1016/j.cossms.2009.01.002.
[30] S. Huang, J. Zhong, J. Li, J. Chen, Z. Xiang, M. Li, Q. Liao, Charge separation and photocatalytic properties of BiOI prepared by ionic liquid-assisted hydrothermal method, Mater. Lett. 183 (2016) 248–250, https://doi.org/10.1016/j.matlet.2016.07.119.
[31] Z. Chen, J. Zeng, J. Di, D. Zhao, M. Ji, J. Xia, H. Li, Facile microwave-assisted ionic liquid synthesis of sphere-like BiOBr hollow and porous nanostructures with enhanced photocatalytic performance, Green, Energy Environ. 2 (2017) 124–133, https://doi.org/10.1016/j.gee.2017.01.005.
[32] Z.-D. Wei, R. Wang, Hierarchical BiOBr microspheres with oxygen vacancies synthesized via reactable ionic liquids for dyes removal, Chin. Chem. Lett. 27 (2016) 769–772, https://doi.org/10.1016/j.cclet.2016.03.013.
[33] J. Xia, Y. Ge, J. Di, L. Xu, S. Yin, Z. Chen, P. Liu, H. Li, Ionic liquid-assisted strategy for bismuth-rich bismuth oxybromides nanosheets with superior visible light-driven photocatalytic removal of bisphenol-A, J. Colloid Interface Sci. 473 (2016) 112–119, https://doi.org/10.1016/j.jcis.2016.03.046.
[34] M. Tański, M. Paszkiewicz, J. Dołżonek, M. Flejszar, A. Bielicka-Giełdon, P. Stepnowski, A. Białk-Bielinska, Regeneration and reuse of the carbon nanotubes for the adsorption of selected anticancer drugs from water matrices, Colloids Surf. A Physicochem. Eng. Asp 618 (2021) 126355, https://doi.org/10.1016/j.colsurfa.2021.126355.
[35] C. Liu, H. Chen, K. Dai, A. Xue, H. Chen, Q. Huang, Synthesis, characterization and its photocatalytic activity of double-walled carbon nanotubes-TiO_2 hybrid, Mater. Res. Bull. 48 (2013) 1499–1505, https://doi.org/10.1016/j.materresbull.2012.12.059.
[36] H. Wu, J. Guo, D. Yang, Facile autoreduction synthesis of core-shell Bi-Bi_2O_3/CNT with 3-dimensional neural network structure for high-rate performance supercapacitor, J. Mater. Sci. Technol. 47 (2020) 169–176, https://doi.org/10.1016/j.jmst.2020.02.007.
[37] S. Wu, Y. Su, Y. Zhu, Y. Zhang, M. Zhu, *In-Situ* growing Bi/BiOCl microspheres on Ti_3C_2 nanosheets for upgrading visible-light-driven photocatalytic activity, Appl. Surf. Sci. 520 (2020) 146339, https://doi.org/10.1016/j.apsusc.2020.146339.
[38] M. Gao, D. Zhang, X. Pu, K. Ding, H. Li, T. Zhang, H. Ma, Combustion synthesis of Bi/BiOCl composites with enhanced electron-hole separation and excellent visible light photocatalytic properties, Sep. Purif. Technol. 149 (2015) 288–294, https://doi.org/10.1016/j.seppur.2015.06.002.
[39] W.W. Lee, C.-S. Lu, C.-W. Chuang, Y.-J. Chen, J.-Ya. Fu, C.-W. Siao, C.-C. Chen, Synthesis of bismuth oxyiodides and their composites: characterization, photocatalytic activity, and degradation mechanisms, RSC Adv. 5 (2015) 23450–23463, https://doi.org/10.1039/c4ra15072d.
[40] K.-L. Li, W.W. Lee, C.-S. Lu, Y.-M. Dai, S.-Y. Chou, H.-L. Chen, H.-P. Lin, C.-C. Chen, Synthesis of BiOBr, Bi_3O_4Br, $Bi_{12}O_{17}Br_2$ by controlled hydrothermal methods and their photocatalytic properties, J. Taiwan Inst. Chem. Engineers 45 (5) (2014) 2688–2697, https://doi.org/10.1016/j.jtice.2014.04.001.
[41] S. Heidari, M. Haghighi, M. Shabani, Sunlight-activated BiOCl/BiOBr–$Bi_{24}O_{31}Br_{10}$ photocatalyst for the removal of pharmaceutical compounds, J. Clean. Prod. 259 (2020) 120679, https://doi.org/10.1016/j.jclepro.2020.120679.
[42] D. Liu, W. Yao, J. Wang, Y. Liu, M. Zhang, Y. Zhu, Enhanced visible light photocatalytic performance of a novel heterostructured $Bi_4O_5Br_2$/$Bi_{24}O_{31}Br_{10}$/Bi_2SiO_5 photocatalyst, Appl. Catal. B 172–173 (2015) 100–107, https://doi.org/10.1016/j.apcatb.2015.01.037.
[43] Y. Peng, P.-P. Yu, Q.-G. Chen, H.-Y. Zhou, A.-W. Xu, Facile fabrication of $Bi_{12}O_{17}Br_2$/$Bi_{24}O_{31}Br_{10}$ type II heterostructures with high visible photocatalytic activity, J. Phys. Chem. C 119 (23) (2015) 13032–13040, https://doi.org/10.1021/acs.jpcc.5b02132.
[44] N. Sharma, Z. Pap, S. Garg, K. Hernádi, Hydrothermal synthesis of BiOBr and BiOBr/CNT composites, their photocatalytic activity and the importance of early $Bi_6O_6(OH)_3(NO_3)_3$•1.5H_2O formation, Appl. Surf. Sci. 495 (2019) 143536, https://doi.org/10.1016/j.apsusc.2019.143536.
[45] C. Zhou, J. Kong, H. Dai, Electrical measurements of individual semiconducting single-walled carbon nanotubes of various diameters, Appl. Phys. Lett. 76 (2000) 1597, https://doi.org/10.1063/1.126107.
[46] F. Li, Q. Wang, J. Ran, Y. Hao, X. Wang, D. Zhao, S.Z. Qiao, Ionic liquid self-combustion synthesis of BiOBr/$Bi_{24}O_{31}Br_{10}$ heterojunctions with exceptional visible-light photocatalytic performances, Nanoscale 7 (3) (2015) 1116–1126, https://doi.org/10.1039/c4nr05451b.
[47] S. Yin, J. Di, M. Li, W. Fan, J. Xia, H. Xu, H. Li, Synthesis of multiwalled carbon nanotube modified BiOCl microspheres with enhanced visible-light response photoactivity, CLEAN - Soil, Air, Water 44 (7) (2016) 781–787, https://doi.org/10.1002/clen.201500418.
[48] Y. Pan, D. Wu, The rGO/BiOBr/$Bi_4O_5Br_2$ composites with stacked nanosheets for ciprofloxacin photodegradation under visible light irradiation, J. Inorg. Gen. Chem. 645 (2019) 1153–1160, https://doi.org/10.1002/zaac.201900115.
[49] R. Pati, Y. Zhang, S.K. Nayak, P.M. Ajayan, Effect of H_2O adsorption on electron transport in a carbon nanotube, Appl. Phys. Lett. 81 (14) (2002) 2638–2640, https://doi.org/10.1063/1.1510969.
[50] J.H. Back, M. Shim, pH-Dependent electron-transport properties of carbon nanotubes, J. Phys. Chem. B 110 (47) (2006) 23736–23741, https://doi.org/10.1021/jp063260x.
[51] Q.W. Li, Y. Li, X.F. Zhang, S.B. Chikkannanavar, Y.H. Zhao, A.M. Dangelewicz, L. X. Zheng, S.K. Doorn, Q.X. Jia, D.E. Peterson, P.N. Arendt, Y.T. Zhu, Structure-dependent electrical properties of carbon nanotube fibers, Adv. Mater. 19 (20) (2007) 3358–3363, https://doi.org/10.1002/adma.200602966.
[52] C. Zhou, J. Kong, H. Dai, Electrical measurements of individual semiconducting single-walled carbon nanotubes of various diameters, Appl. Phys. Lett. 76 (12) (2000) 1597–1599, https://doi.org/10.1063/1.126107.